The Astrophysical Journal Letters, 816:L20 (6pp), 2016 January 10 doi:10.3847/2041-8205/816/2/L20

GAMMA-RAY BURSTS FROM MAGNETIC RECONNECTION: VARIABILITY AND ROBUSTNESS OF LIGHT CURVES

Jonathan Granot
Department of Natural Sciences, The Open University of Israel, 1 University Road, P.O. Box 808, Ra'anana 4353701, Israel
Received 2015 October 27; accepted 2015 December 19; published 2016 January 6

ABSTRACT

The dissipation mechanism that powers gamma-ray bursts (GRBs) remains uncertain almost half a century after their discovery. The two main competing mechanisms are the extensively studied internal shocks and the less studied magnetic reconnection. Here we consider GRB emission from magnetic reconnection accounting for the relativistic bulk motions that it produces in the jet's bulk rest frame. Far from the source the magnetic field is almost exactly normal to the radial direction, suggesting locally quasi-spherical thin reconnection layers between regions of oppositely directed magnetic field. We show that if the relativistic motions in the jet's frame are confined to such a quasi-spherical uniform layer, then the resulting GRB light curves are independent of their direction distribution within this layer. This renders previous results for a delta-function velocity-direction distribution applicable to a much more general class of reconnection models, which are suggested by numerical simulations. Such models that vary in their velocity-direction distribution differ mainly in the size of the bright region that contributes most of the observed flux at a given emission radius or observed time. The more sharply peaked this distribution, the smaller this bright region, and the stronger the light curve variability that may be induced by deviations from a uniform emission over the thin reconnection layer, which may be expected in a realistic GRB outflow. This is reflected both in the observed image at a given observed time and in the observer-frame emissivity map at a given emission radius, which are calculated here for three simple velocity-direction distributions.

Key words: gamma-ray burst: general – magnetic reconnection – magnetohydrodynamics (MHD) – methods: analytical – relativistic processes

1. INTRODUCTION

Gamma-ray Bursts (GRBs) are the most luminous cosmic explosions, with huge isotropic-equivalent luminosities of $L_{\rm iso} \sim 10^{50} - 10^{53}$ erg s^{-1} (for a review see, e.g., Piran 2004; Kumar & Zhang 2015). They divide into two main sub-classes (Kouveliotou et al. 1993): long-duration ($\gtrsim$2 s) soft-spectrum GRBs that are associated with broad-lined SNe Ic, implying a massive-star progenitor (e.g., Woosley & Bloom 2006), and short-duration ($\lesssim$2 s) hard-spectrum GRBs that are thought to arise from the merger of a binary neutron-star system or a neutron star and a stellar-mass black hole (Eichler et al. 1989; Narayan et al. 1992; Lee & Ramirez-Ruiz 2007; Nakar 2007). In both classes the central engine is a newly formed rapidly accreting stellar-mass black hole or a rapidly rotating highly magnetized neutron star (millisecond magnetar), which launches a relativistic jet.

The bright GRB prompt γ-ray emission shows rapid variability and typically peaks at photon energies of hundreds of keV. This would imply a huge optical depth to pair production, which is incompatible with its non-thermal spectrum (the compactness problem), unless the emitting region moves toward us with an ultra-relativistic Lorentz factor of $\Gamma \gtrsim 100$ (Baring & Harding 1997; Lithwick & Sari 2001; Granot et al. 2008; Hascoët et al. 2012). Such a highly relativistic outflow also naturally explains the subsequent afterglow emission in X-ray, optical and radio over days, weeks and months after the GRB, as the ejecta are decelerated by the external medium and drive a long-lived shock into it, which gradually decelerates as it sweeps-up more mass. Compactness arguments also require a large enough prompt emission radius ($\sim 10^{13} - 10^{16}$ cm) in particular for the $\sim$ GeV photons detected by *Fermi* in some GRBs (e.g., Abdo et al. 2009, 2010; Ackermann et al. 2013). The observed fast variability of the GRB prompt emission implies that it must be produced by internal dissipation within the ejecta (Sari & Piran 1997).

The GRB outflow composition, as well as the dissipation and emission mechanisms that produce the prompt emission are still uncertain, and are important open questions in this field. They can also affect each other, as the outflow composition affects its dynamics and dissipation, which in turn affect the resulting emission. In particular, a key question is whether the energy is carried out from the central source to the emission region predominantly as kinetic energy—a baryonic jet (Goodman 1986; Paczýnski 1986; Shemi & Piran 1990), or as Poynting flux—a highly magnetized (or Poynting-flux dominated) jet (Usov 1992; Thompson 1994; Mészáros & Rees 1997; Blandford 2002; Lyutikov 2006; Granot et al. 2015) with a large magnetization parameter σ (the magnetic-to-particle enthalpy density or energy flux ratio). A baryonic, kinetically dominated jet can naturally lead to reasonably efficient energy dissipation via internal shocks within the outflow (Rees & Mészáros 1994). This may also occur in an initially high-σ outflow that is highly variably, due to impulsive acceleration that converts its initial magnetic energy into kinetic energy (Granot et al. 2011; Granot 2012). As long as the flow remains highly magnetized this suppresses internal shocks. On the other hand, in high-σ outflows there is an alternative dissipation mechanism that can be more efficient than internal shocks—magnetic reconnection (Thompson 1994; Spruit et al. 2001; Lyutikov & Blandford 2003; Giannios & Spruit 2007; Lyubarsky 2010; Kagan et al. 2015).

A high σ near the central source can help avoid excessive baryon loading that might prevent the jet from reaching sufficiently high Lorentz factors far from the source, at the emission region. Such initially high-σ jets are also favored on

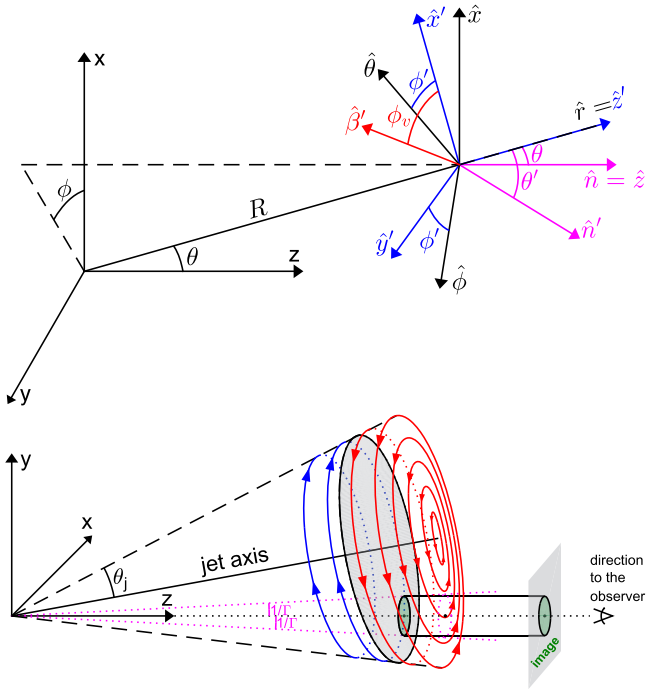

Figure 1. Schematic geometry of our model. Bottom: our basic model features shells of oppositely oriented toroidal magnetic field (in blue and red), separated by a locally quasi-spherical thin reconnection layer (in gray). The observed region of angle $\sim 1/\Gamma$ around the line of sight (in green) that contributes to the observed image and flux is a small part of the jet. Top: the unprimed source rest frame (in black) is shown in Cartesian (x, y, z) and spherical (R, θ, ϕ) coordinates, where $\hat{z}$ points to the observer. The primed, jet's bulk frame (in blue) is the local rest frame of a point on a spherical emitting shell of radius R expanding radially with Lorentz factor $\Gamma \gg 1$. The velocity direction $\hat{\beta}'$ (in red) of the emitting plasma in the primed frame is in the x'–y' plane (normal to the radial direction) at an angle ϕ_v from $\hat{x}'$ (the local magnetic-field direction before reconnection). Also shown (in magenta) are the directions of a photon that reaches the observer in both frames (which are related through aberration of light).

energetic grounds, since modeling of GRB central engines that rely on hydromagnetic jet launching via accretion disks suggest that their power is significantly larger than that of thermally driven outflows powered by neutrino-anti neutrino annihilation (e.g., Kawanaka et al. 2013), and they may naturally lead to magnetic reconnection.

In a striped wind magnetic field configuration (e.g., Coroniti 1990), whether the flipping of the magnetic field direction near the source is periodic (as expected for a millisecond-magnetar central engine) or stochastic (as expected for an accreting black hole), reconnection at large distances from the source has a natural preferred direction. At such large distances the magnetic field is almost exactly normal to the (spherical) radial direction, as are the current sheets that separate regions of opposite magnetic polarity where reconnection occurs, thus forming nearly spherical thin reconnection layers. Moreover, for a large σ just before the dissipation region reconnection leads to local relativistic bulk motion of the outgoing particles away from the reconnection sites in the jet's bulk frame, with a Lorentz factor Γ' that can reach a few to several. This leads to anisotropic emission in the jet's bulk frame, which can significantly affect the observed emission.

Figure 1 (bottom panel) shows a simple manifestation of our basic model where the jet consists of shells with oppositely oriented toroidal magnetic field, separated by quasi-spherical current sheets where reconnection occurs (a modest poloidal field-component should not significantly change this basic picture). In GRBs the jet half-opening angle typically satisfies $\theta_j \gg 1/\Gamma$ so only a small fraction of the jet ($\sim(\Gamma\theta_j)^{-2} \ll 1$; the green circle in Figure 1) is visible, and the magnetic field may be approximated as uniform within it. This approximation was made for calculating the prompt-GRB polarization (Granot 2003; Granot & Königl 2003), and should not greatly affect our results. For the afterglow polarization the global toroidal-field structure was considered (Lazzati et al. 2004; Granot & Taylor 2005) since the whole jet becomes visible as it decelerates during the afterglow. Anisotropic synchrotron emission was considered as a possible cause of early X-ray afterglow variability or rapid decay (Beloborodov et al. 2011). We allow for any reconnection-induced velocity-direction distribution in the jet's bulk frame $g(\phi_v)$ within the quasi-spherical reconnection layer (ϕ_v is defined in Figure 1, top panel). Such an anisotropic emission model was recently considered for the prompt-GRB emission by Beniamini & Granot (2016, hereafter BG16), where velocities are in the direction of the anti-parallel magnetic-field lines just prior to their reconnection, which is uniform within visible region.

Our anisotropic emission model differs from previous relativistic-turbulence models (Lyutikov & Blandford 2003; Kumar & Narayan 2009; Lazar et al. 2009) that assume an isotropic velocity distribution of the motions in the jet's bulk frame. For this model BG16 calculated the expected light curves and spectra of the prompt emission, and demonstrated that it can potentially reproduce many of the observed prompt GRB properties (e.g., its variability, pulse asymmetry, the very rapid decay phase at its end, and many of the observed correlations).

Recent simulations of relativistic magnetic reconnection suggest that as σ increases, both the reconnection rate and resulting particle bulk velocities (β') increase, and the power-law index of their energy spectrum becomes harder (Cerutti et al. 2012, 2014; Sironi & Spitkovsky 2014; Guo et al. 2015; Kagan et al. 2015; Liu et al. 2015). In high-σ GRB outflows one may typically expect $\Gamma' \sim$ a few to several. The collimation of the accelerated electrons appears to increase with their energy. Their velocities are indeed predominantly confined to the reconnection layer, but are not necessarily along the anti-parallel directions of the magnetic field lines just before the reconnection (as was assumed by BG16). This motivates us to consider such velocity distributions that are more general.

In Section 2 the light curve is shown to be independent of the angular distribution $g(\phi_v)$ of the velocities in the jet's bulk frame as long as they are confined to a uniformly emitting spherical reconnection layer; $g(\phi_v)$ does, however, affect the observed image and the contribution to the observed flux from a given emission radius, which are calculated in Section 3 and Section 4, respectively. This may in turn affect the prompt GRB light curve if the emission across the spherical reconnection layer is non-uniform, which may be expected under realistic conditions. Finally, the main results are summarized and discussed in Section 5.

2. FLUX DENSITY IS INDEPENDENT OF VELOCITY DIRECTIONS WITHIN A UNIFORM SPHERICAL RECONNECTION LAYER

Here we show that the observed flux density $F_\nu(T)$ at any observed frequency ν and time T is independent of the velocity-direction distribution of the emitting plasma within a uniform spherical thin reconnection layer. Let $g(\phi_v)$ be such a general

probability distribution (normalized as $\int_0^{2\pi} g(\phi_v)d\phi_v = 1$) of local velocity directions in the jet's bulk frame (that is primed in Figure 1, top panel) that are at angles ϕ_v relative to the local direction of the magnetic field ($\hat{x}'$ in Figure 1, which is a preferred direction within the reconnection layer, and is assumed here to be uniform within the visible region). We follow the notations of BG16 (e.g., in the source's frame θ is the polar angle measured from the line of sight, and ϕ is the azimuthal angle). The general expression for the flux density is then given by a weighted average over that for a single velocity direction taken from BG16,

$$F_\nu(T) = \frac{L''_{\nu''_0}}{(4\pi D)^2}\int dy \left|\frac{d\mu}{dy}\right| \mathcal{D}^3(y) f\left[y\left(\frac{T}{T_0}\right)^{\frac{1}{m+1}}\right] \times \int_0^{2\pi} d\phi \int_0^{2\pi} d\phi_v\, g(\phi_v) S(x) \frac{\mathcal{D}'^{\,3-k}}{\Gamma'^{\,k}}, \quad (1)$$

where $D = d_L(1+z)^{-1/2}$ is the effective distance to the source and $d_L(z)$ is the luminosity distance, $y = R/R_L$ is the normalized radius, $k = 0$ for a blob and $k = 1$ for a steady state in the jet's frame, $\mu = \cos\theta$, $\mathcal{D}(y) = 1/\Gamma(1-\beta\mu)$ is the Doppler factor between the rest frame of the central source and the jet's bulk frame, $\mathcal{D}' = 1/\Gamma'[1-\beta'\sin\theta'\cos(\phi-\phi_v)]$ is the Doppler factor between the jet's bulk frame and the local emitting plasma's rest frame (it depends on y through θ'), and $x = \nu''/\nu''_0(y) = \nu_z/[\mathcal{D}\mathcal{D}'\nu''_0(y)]$ where $\nu_z = (1+z)\nu$ is the frequency in the source's cosmological frame. Thus, the only dependence on the azimuthal angle ϕ is through $\mathcal{D}'$, both directly and through x, and this dependence is in turn only through $\varphi \equiv \phi - \phi_v$. Therefore, one can reverse the order of integration over ϕ and ϕ_v, and change variables from ϕ to φ,

$$\int_0^{2\pi} d\phi_v g(\phi_v) \int_0^{2\pi} d\varphi\, S[x(\varphi)] \frac{\mathcal{D}'^{\,3-k}(\varphi)}{\Gamma'^{\,k}}, \quad (2)$$

where the inner integral over φ is independent of ϕ_v, so that the outer integral over ϕ_v gives 1 from the normalization of $g(\phi_v)$. This reduces the expression for the observed flux density to that for a delta function in velocity direction (e.g., $g_1(\phi_v)$ in Equation (4)) as in BG16, where one can take $\phi_v = 0$,

$$F_\nu(T) = \frac{L''_{\nu''_0}}{(4\pi D)^2}\int dy \left|\frac{d\mu}{dy}\right| \mathcal{D}^3 f(y) \int_0^{2\pi} d\phi S(x) \frac{\mathcal{D}'^{\,3-k}}{\Gamma'^{\,k}}. \quad (3)$$

The reason why the observed flux is independent of $g(\phi_v)$ is as follows. The observed flux is the weighted mean of the contributions from plasma with different velocity directions ϕ_v. However, the observed flux from such a uni-directional distribution does not depend on its absolute direction ϕ_v, since the latter affects only the dependence of the observed radiation on the azimuthal angle ϕ, and thus the observed image, but not the photon arrival times or the observed flux density.

3. THE OBSERVED IMAGE FOR ANISOTROPIC EMISSION

This motivates us to calculate the observed image for different choices of $g(\phi_v)$ and Γ'. For comparison we will also show the image for isotropic emission in the jet's bulk frame ($\Gamma' = 1$), from Granot (2008). In particular, we will use

$$g_1(\phi_v) = \frac{\delta(\phi_v) + \delta(\phi_v - \pi)}{2},$$
$$g_2(\phi_v) = \frac{\cos^2\phi_v}{\pi}, \quad g_3(\phi_v) = \frac{1}{2\pi}, \quad (4)$$

where $g_1(\phi_v)$ (used in BG16) corresponds to velocity along the anti-parallel reconnecting magnetic field lines, $g_2(\phi_v)$ is motivated by PIC simulations of relativistic reconnection, and $g_3(\phi_v)$ is the extreme assumption of a uniform velocity distribution within the thin reconnection layer. For each of these $g(\phi_v)$ we calculate the image for $\Gamma' = 1, 2, 4, 8$.

The flux density differential is $dF_\nu = I_\nu d\Omega = I_\nu dS_\perp/d_A^2$, where $d_A(z)$ is the angular distance to the source and $S_\perp$ is the area of the image, normal to the line of sight. If $R_\perp$ is the corresponding distance from the center of the image, then

$$dS_\perp = R_\perp dR_\perp d\phi = \left(\frac{R_L}{\Gamma_L}\right)^2 \frac{[1-(m+2)y^{m+1}]}{2(m+1)} dy d\phi, \quad (5)$$

where $\Gamma^2 \propto R^{-m}$. We are interested in the specific intensity at a general location within the image, $I_\nu(r, \phi)$, where

$$r \equiv \frac{R_\perp}{R_{\perp,\max}} = \frac{(m+2)^{\frac{m+2}{2(m+1)}}}{\sqrt{m+1}}\sqrt{y - y^{m+2}}, \quad (6)$$

and $R_{\perp,\max} = (m+2)^{-(m+2)/[2(m+1)]} R_L/\Gamma_L$. As we evaluate I_ν at a fixed ϕ, one still needs to integrate over ϕ_v, or more conveniently switch variables to φ and obtain

$$\frac{dF_\nu}{dy d\phi} = \frac{L''_{\nu''_0}}{(4\pi D)^2}\left|\frac{d\mu}{dy}\right| \mathcal{D}^3 f(y) \int_0^{2\pi} d\varphi\, \frac{g(\phi-\varphi)S[x(\varphi)]}{\Gamma'^{\,k}\mathcal{D}'^{\,k-3}(\varphi)}, \quad (7)$$

$$I_\nu = \frac{L''_{\nu''_0}}{(4\pi)^2}\frac{\mathcal{D}^3 f(y)}{(1+z)^3}\left|\frac{d\mu}{dy}\right| \left(\frac{\Gamma_L}{R_L}\right)^2 \frac{2(m+1)}{|1-(m+2)y^{m+1}|} \times \int_0^{2\pi} d\varphi\, \frac{g(\phi-\varphi)S[x(\varphi)]}{\Gamma'^{\,k}\mathcal{D}'^{\,k-3}(\varphi)}. \quad (8)$$

Now we shall use the expressions for the relevant terms,

$$\left|\frac{d\mu}{dy}\right| = \frac{y^{-2} + m y^{m-1}}{2(m+1)\Gamma_L^2}, \quad \mathcal{D} = \Gamma_L \frac{2(m+1)y^{-m/2}}{m + y^{-m-1}}, \quad (9)$$

$$\mathcal{D}'(\varphi) = \frac{1}{\Gamma'}\left(1 - 2\beta'\frac{\sqrt{(m+1)(y^{-m-1}-1)}}{m+y^{-m-1}}\cos\varphi\right)^{-1}. \quad (10)$$

Now, for simplicity, we shall specify to a power-law spectrum, $S(x) = x^{-\alpha}$, and emission with radius, $f(R/R_0) \propto R^a$ between R_0 and $R_f = R_0 + \Delta R$, with a constant Γ' and ν''_0,[1]

$$I_\nu \propto \frac{\nu^{-\alpha} T^{\frac{2a-4-m(3+\alpha)}{2(m+1)}} y^{a-1-\frac{m}{2}(1+\alpha)}}{(m+y^{-m-1})^{2+\alpha}\left|1 - \frac{m+2}{y^{-m-1}}\right|}\int_0^{2\pi} \frac{g(\phi-\varphi)d\varphi}{\mathcal{D}'^{\,k-3\alpha(\varphi)}}. \quad (11)$$

[1] This result reduces to Equation (15) of Granot (2008) for isotropic emission in the jet's bulk frame ($\Gamma' = 1$), with the small modifications given in Equations (8) and (17) therein, which reflect the difference between a shock and a reconnection layer. To match the notations there one should take $\alpha \to -b$ and $m \to 3-k$ where there k is the power-law index of the external density profile in front of the afterglow shock.

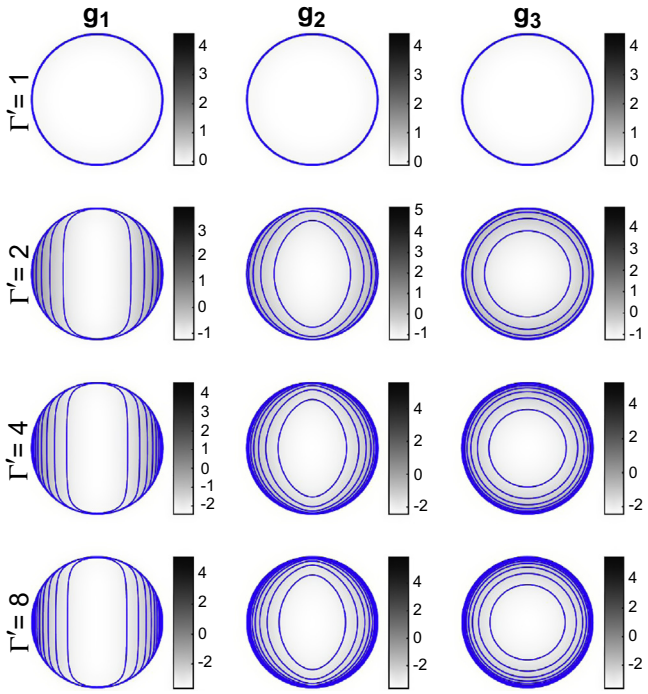

Figure 2. Images (according to Equation (11), corresponding to the green region in Figure 1, bottom panel) for different velocity distributions within the reconnection layer (functions g_1, g_2 and g_3 in Equation (4), from left to right), and for different values of Γ' (=1, 2, 4, 8 from top to bottom), for $m = 0$ ($\Gamma \propto R^{-m/2}$), $k = 1$ (steady-state reconnection in the jet's bulk frame), $a = 0$ and $\alpha = 1$ ($L''_{\nu''} \propto R^a (\nu'')^{-\alpha}$). Shown are logarithmic maps of the specific intensity normalized by its mean value in the image, $\log_{10}(I_\nu/\langle I_\nu \rangle)$, with contours at $\log_{10}[I_\nu/\min(I_\nu)] = 0.5, 1, 1.5, \ldots$.

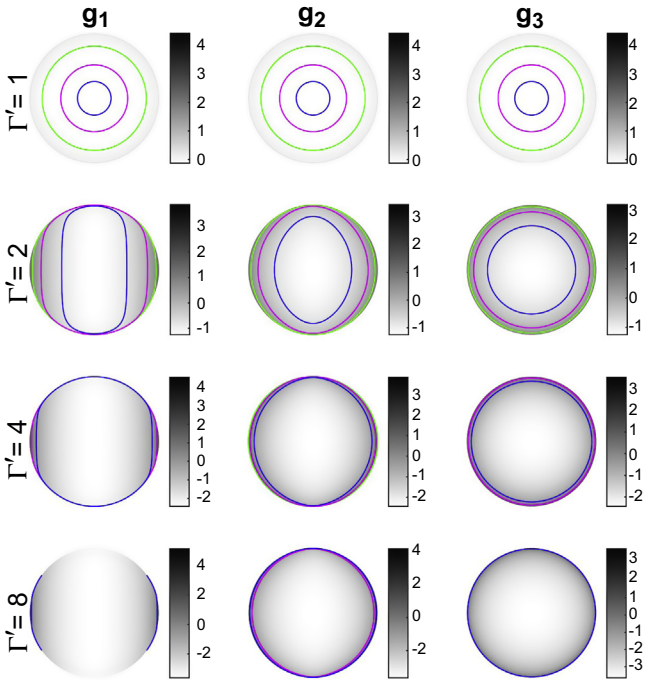

Figure 3. Similar to Figure 2, but showing contour lines for which 50% (green), 80% (magenta), and 95% (blue) of the total flux comes from higher I_ν values, i.e., from the region between the contour and the outer edge of the image.

Each $r < 1$ corresponds to two values of y, at the front (y_+) and the back (y_-) of the equal arrival time surface of photons to the observer. They are generally found by numerically solving Equation (6), but for some m-values $y_\pm(r; m)$ can be found analytically (Granot 2008), e.g., $y_\pm(r; 0) = \frac{1}{2}(1 \pm \sqrt{1 - r^2})$ and $y_\pm(r; 1) = (2/\sqrt{3})\cos\left[\frac{1}{3}(\pi \mp \arctan\sqrt{r^{-4} - 1})\right]$. One must add up these two contributions to $I_\nu(r, \phi)$. There is contribution only from radii $R_0 \leqslant R \leqslant R_f$ corresponding to $y_{\min} \leqslant y \leqslant y_{\max}$ where $y_{\min} = \min[1, R_0/R_L(T)]$ and $y_{\max} = \min[1, R_f/R_L(T)]$. In the following, for simplicity, emission is assumed from all radii.

The resulting images are shown in Figures 2 and 3. Figure 2 adds equally spaced contour lines, with $\Delta \log_{10}(I_\nu) = 0.5$. Figure 3 adds contour lines at I_ν values above which 50% (green), 80% (magenta), and 95% (blue) of the total flux originates. For $\Gamma' \gtrsim 2$ most of the flux clearly comes from a small part of the image near its outer edge. For $g_1(\phi_v)$ (a delta-function anti-parallel velocity distribution) most of the flux comes from two small regions near the outer edge of the image, which quickly decrease in size as Γ' increases. For $g_2(\phi_v) = \frac{1}{\pi}\cos^2\phi_v$ most of the flux comes from an asymmetric ring at the outer edge of the image. For $g_3(\phi_v) = 1/2\pi$ (an isotropic velocity distribution within the reconnection layer – normal to the radial direction) this ring becomes symmetric about the center of the image, following the behavior of the whole image in this case for which there is no preferred ϕ-direction.

4. CONTRIBUTION TO OBSERVED FLUX FROM A GIVEN RADIUS

It is also useful to examine the contribution to the observed flux from a given emission radius R (as a function of θ and ϕ) even though it arrives over a range of observed times T. To this end we consider the contribution per unit area of the shell $dA = R^2 d\mu d\phi$ at a constant R and $\Gamma = \Gamma(R)$, where

$$\mathcal{D} = \frac{2\Gamma}{1 + (\Gamma\theta)^2}, \quad \mathcal{D}' = \frac{1}{\Gamma'\left(1 - \beta'\frac{2(\Gamma\theta)}{1 + (\Gamma\theta)^2}\cos\phi\right)}. \tag{12}$$

Altogether, for a power-law emission spectrum one obtains

$$\frac{dF_\nu}{d\mu d\phi} \propto \frac{\nu^{-\alpha}}{[1 + (\Gamma\theta)^2]^{3+\alpha}} \times \int_0^{2\pi} \frac{g(\phi - \varphi)d\varphi}{\left(1 - \frac{2(\Gamma\theta)\beta'}{1 + (\Gamma\theta)^2}\cos\varphi\right)^{3+\alpha-k}}. \tag{13}$$

The integrals over φ in Equations (11) and (13), $G_j(\phi)$ for $g_j(\phi - \varphi)$, generally give hypergeometric functions for $j = 2, 3$. However, for integer $\alpha - k$ values they become particularly simple. E.g., for $\alpha - k = 0$, $G_3(\phi) \propto (1 - B)^{-5/2}(2 + B)$ and $G_2(\phi) \propto (1 - B)^{-5/2}(2 + B[1 + 3\cos(2\phi)])$, where

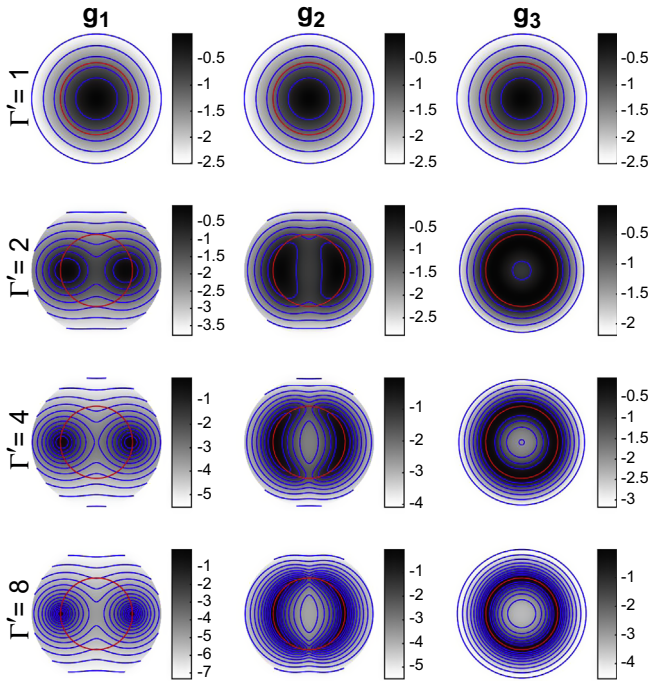

Figure 4. Logarithmic maps of the (normalized) contribution to the observed flux density per unit area of the shell at a given radius R, $\log_{10}[(dF_\nu/dA)/\max(F_\nu/dA)]$ according to Equation (13), for different velocity distributions within the reconnection layer (functions g_1, g_2 and g_3 in Equation (4), from left to right), and for different values of Γ' (=1, 2, 4, 8 from top to bottom), for $m = 0$, $k = 1$, $a = 0$ and $\alpha = 1$. The contour lines are at $-\log_{10}[(dF_\nu/dA)/\max(F_\nu/dA)] = 0.5, 1, 1.5, \ldots$. A red circle is added at $\theta = 1/\Gamma(R)$ for reference.

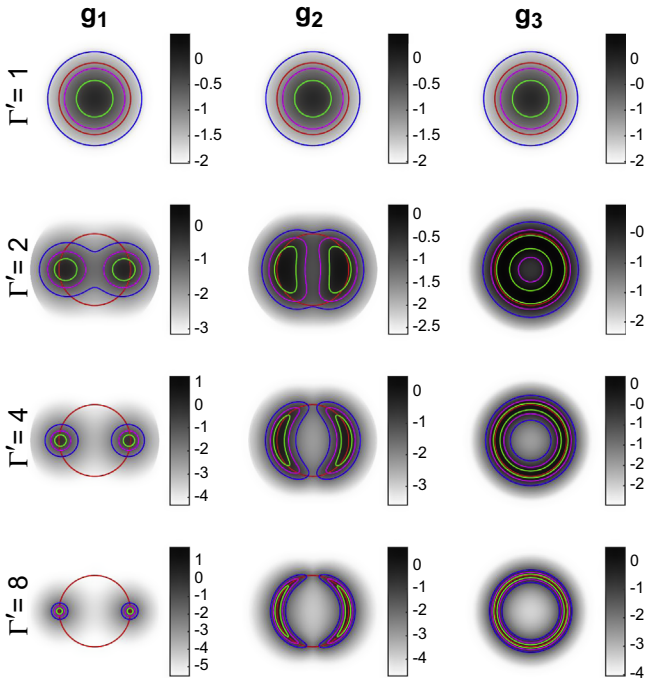

Figure 5. Similar to Figure 4, but showing contour lines at the dF_ν/dA values above which 50% (green), 80% (magenta), and 95% (blue) of the total flux from the given emission radius originates, corresponding to the regions enclosed by these contours.

$B = (\beta' \sin\theta')^2$ is given by

$$B = \begin{cases} \left(\dfrac{2\beta'}{m + y^{-m-1}}\right)^2 (m+1)(y^{-m-1} - 1) & \text{(Equation (11))}, \\ 4(\beta')^2(\Gamma\theta)^2[1 + (\Gamma\theta)^2]^{-2} & \text{(Equation (13))}. \end{cases} \quad (14)$$

Figures 4 and 5 show logarithmic color maps of dF_ν/dA, the contribution to the observed flux density per unit area of the emitting shell from a given radius, according to Equation (13). Figure 4 adds equally spaced contour lines, with $\Delta \log_{10}(dF_\nu/dA) = 0.5$. Figure 5 adds contour lines at the dF_ν/dA values above which 50% (green), 80% (magenta), and 95% (blue) of the total flux from the given emission radius originates.

5. DISCUSSION

In Section 2 it was shown that the observed flux density (and thus the light curves and spectra) of GRB prompt emission from a uniform spherical thin reconnection layer are independent of the distribution of velocity β' directions within this layer in the jet's bulk frame. This implies that the detailed results for the light curves, spectra, and temporal-spectral correlations of BG16, who assumed velocities along two anti-parallel directions, are valid for a much larger class of reconnection models, which is consistent with the results of recent simulations.

In Sections 3 and 4 it was shown that as Γ' increases, the size of the "bright part" within the observed region of the reconnection layer that contributes most of the observed flux becomes significantly smaller. Moreover, its area and angular size depend on the spread of $\hat{\beta}'$, as expressed in the angular distribution $g(\phi_v)$. For $\Gamma' \gtrsim$ a few, for the tightest angular distribution we considered of two anti-parallel directions (g_1 in Equation (4)) most of the observed flux comes from two small circular regions of angular size $\sim 1/(\Gamma'\Gamma)$ (see left panels of Figure 5), which occupy a fraction $\sim \Gamma'^{-2}$ of the visible region. On the other extreme, for our most spread-out velocity distribution that is uniform within the reconnection layer (g_3 in Equation (4)), most of the flux comes from a thin ring of angular radius $1/\Gamma$ and width $\sim 1/(\Gamma'\Gamma)$ (see right panels of Figure 5), occupying a fraction $\sim 1/\Gamma'$ of the visible region. These results should not significantly change when relaxing our approximation of a uniform magnetic field within the visible region.

These results may be important if the emission over the spherical thin reconnection layer is not uniform but has some angular dependence, e.g., due to irregularities or non-uniformity in the reconnection rate. The value of σ affects Γ' (which determines the size of the region contributing most of the observed flux), the reconnection rate (which affects the local radiated power per unity area in the reconnection layer), as well as the electron energy distribution that affects the emission spectrum (and hence the observed spectrum and flux at a given observed energy range). Since σ may vary with the angular location within the outflow, or even with time at a fixed angular location, one might expect that this could potentially lead to significant angular inhomogeneities in the emission from a given radius, as well as temporal changes at a given angular location.

If the prompt emission occurs when the jet is coasting at a constant Γ then the angular location of the "bright part" (which is at an angle of $1/\Gamma$ from the line of sight) is fixed in time and the light curve variability reflects mainly the radial profile of the emission within this small region. If, on the other hand, the jet is still accelerating or conversely starting to decelerate during the reconnection, then the "bright part" will scan through different angular locations and the light curve variability could also reflect the angular distribution of the spectral emissivity in the reconnection layer. In all cases, the larger this "bright part" (i.e., the smaller Γ' or σ, and the wider the velocity spread $g(\phi_v)$) the more it might average out over different local fluctuations or angular inhomogeneities in the emission, thus reducing the light curve variability. Conversely, a larger light curve variability may be expected for a smaller "bright part" (i.e., a larger Γ' or σ, and a narrower velocity spread $g(\phi_v)$), due to less averaging out, and a larger sensitivity to fluctuations in the emission over small times or angular scales. A more detailed and quantitative study of these effects on the observed prompt GRB emission is planned in a future work.

J.G. thanks Paz Beniamini for useful comments, and acknowledges support from the ISF grant 719/14.

REFERENCES

Abdo, A. A., Ackermann, M., Ajello, M., et al. 2010, ApJ, 712, 558
Abdo, A. A., Ackermann, M., Asano, K., et al. 2009, ApJ, 707, 580
Ackermann, M., et al. 2013, ApJS, 209, 11
Baring, M. G., & Harding, A. K. 1997, ApJ, 491, 663
Beloborodov, A. M., Daigne, F., Mochkovitch, R., & Uhm, Z. L. 2011, MNRAS, 410, 2422
Beniamini, P., & Granot, J. 2016, MNRAS, submitted (arXiv:1509.02192)
Blandford, R. D. 2002, in Lighthouses of the Universe: The Most Luminous Celestial Objects and Their Use for Cosmology, ed. M. Gilfanov, R. Sunyeav, & E. Churazov (Berlin: Springer), 381
Cerutti, B., Werner, G. R., Uzdensky, D. A., & Begelman, M. C. 2012, ApJL, 754, L33
Cerutti, B., Werner, G. R., Uzdensky, D. A., & Begelman, M. C. 2014, ApJ, 782, 104
Coroniti, F. V. 1990, ApJ, 349, 538
Eichler, D., Livio, M., Piran, T., & Schramm, D. N. 1989, Natur, 340, 126
Giannios, D., & Spruit, H. C. 2007, A&A, 469, 1
Goodman, J. 1986, ApJL, 308, L47
Granot, J. 2003, ApJL, 596, L17
Granot, J. 2008, MNRAS, 390, L46
Granot, J. 2012, MNRAS, 421, 2467
Granot, J., Cohen-Tanugi, J., & do Couto e Silva, E. 2008, ApJ, 677, 92
Granot, J., Komissarov, S. S., & Spitkovsky, A. 2011, MNRAS, 411, 1323
Granot, J., & Königl, A. 2003, ApJL, 594, L83
Granot, J., Piran, T., Bromberg, O., Racusin, J. L., & Daigne, F. 2015, in The Strongest Magnetic Fields in the Universe, Vol. 54, ed. A. Balogh et al. (Berlin: Springer), 471
Granot, J., & Taylor, G. B. 2005, ApJ, 625, 263
Guo, F., Liu, Y.-H., Daughton, W., & Li, H. 2015, ApJ, 806, 167
Hascoët, R., Daigne, F., Mochkovitch, R., & Vennin, V. 2012, MNRAS, 421, 525
Kagan, D., Sironi, L., Cerutti, B., & Giannios, D. 2015, in The Strongest Magnetic Fields in the Universe, Vol. 54, ed. A. Balogh et al. (Berlin: Springer), 545
Kawanaka, N., Piran, T., & Krolik, J. H. 2013, ApJ, 766, 31
Kouveliotou, C., Meegan, C. A., Fishman, G. J., et al. 1993, ApJL, 413, L101
Kumar, P., & Narayan, R. 2009, MNRAS, 395, 472
Kumar, P., & Zhang, B. 2015, PhR, 561, 1
Lazar, A., Nakar, E., & Piran, T. 2009, ApJL, 695, L10
Lazzati, D., Covino, S., Gorosabel, J., et al. 2004, A&A, 422, 121
Lee, W. H., & Ramirez-Ruiz, E. 2007, NJPh, 9, 17
Lithwick, Y., & Sari, R. 2001, ApJ, 555, 540
Liu, Y.-H., Guo, F., Daughton, W., Li, H., & Hesse, M. 2015, PhRvL, 114, 095002
Lyubarsky, Y. E. 2010, ApJL, 725, L234
Lyutikov, M. 2006, NJPh, 8, 119
Lyutikov, M., & Blandford, R. 2003, arXiv:astro-ph/0312347
Mészáros, P., & Rees, M. J. 1997, ApJL, 482, L29
Nakar, E. 2007, PhR, 442, 166
Narayan, R., Paczýnski, B., & Piran, T. 1992, ApJL, 395, L83
Paczýnski, B. 1986, ApJL, 308, L43
Piran, T. 2004, RvMP, 76, 1143
Rees, M. J., & Mészáros, P. 1994, ApJL, 430, L93
Sari, R., & Piran, T. 1997, ApJ, 485, 270
Shemi, A., & Piran, T. 1990, ApJL, 365, L55
Sironi, L., & Spitkovsky, A. 2014, ApJL, 783, L21
Spruit, H. C., Daigne, F., & Drenkhahn, G. 2001, A&A, 369, 694
Thompson, C. 1994, MNRAS, 270, 480
Usov, V. V. 1992, Natur, 357, 472
Woosley, S. E., & Bloom, J. S. 2006, ARA&A, 44, 507